Chemical Science

ROYAL SOCIETY OF CHEMISTRY

EDGE ARTICLE

View Article Online
View Journal | View Issue

Cite this: *Chem. Sci.*, 2025, **16**, 17867

All publication charges for this article have been paid for by the Royal Society of Chemistry

Tuning the dimensionality of functional thiazolo[5,4-*d*]thiazole based supramolecular polymers *via* competitive interactions

Akshay Thorat,[a] Rahul Sahu,[b] Udaijit Pattnaik,[c] Devamrutha Ilayidathu Suresh,[c] Satyaprasad P. Senanayak,*[c] Sandeep K. Reddy*[b] and Chidambar Kulkarni*[a]

Received 28th May 2025
Accepted 26th August 2025

DOI: 10.1039/d5sc03874j

rsc.li/chemical-science

The supramolecular organization of functional molecules at the mesoscopic level influences their material properties. Typically, planar π-conjugated (disc- or linear-shaped) molecules tend to undergo one-dimensional (1D) stacking, whereas two-dimensional (2D) organization from such building blocks is seldom observed in spite of their technological potential. Herein, we rationally achieve both 1D and 2D organizations from a single planar, π-conjugated molecular system *via* competitive interactions. We exemplify this concept through the supramolecular polymerization of amide functionalized thiazolo[5,4-*d*]thiazole chromophores into micron-sized, highly crystalline 2D sheets and 1D nanofibers in a range of different solvents. Solution-grown 2D sheets and 1D nanofibers with intermolecular hydrogen bonding were obtained for *n*-octyl and *n*-hexadecyl chain bearing derivatives, respectively. Molecular dynamics simulations reveal that for *n*-octyl derivatives weak C–H···S and C–H···N interactions between the π-conjugated cores of lateral monomers are dominant leading to 2D sheets, whereas with *n*-hexadecyl chains, enhanced van der Waals interactions of side-chains lead to 1D growth. For intermediate alkyl chain length (*n*-dodecyl), a competition between these two interactions leads to a combination of both 1D nanofibers and 2D sheets. The highly crystalline 2D sheets exhibit over two orders of magnitude higher electrical conductivity compared to their amorphous counterpart. We envisage that the strategy of competitive interaction could potentially be applicable to other heteroatom bearing chromophores to achieve tuneable soft functional materials.

Introduction

The supramolecular assembly of functional monomeric units into high molecular weight polymeric materials *via* non-covalent interactions has been extensively pursued in the past few decades to create soft tuneable materials.[1–5] Various aspects of supramolecular polymerization such as the mechanisms of growth,[6–9] kinetically controlled assembly,[10–13] pathway complexity[11,14,15] and seed-mediated living supramolecular polymerization[16,17] have been studied. However, in most of these reports a disc-shaped π-conjugated core or bi-sfunctionalized linear chromophore is used as the building block, which often results in 1D polymers.[6,18]

On the other hand, controlled synthesis of 2D architectures with potential applications in gas separation and optoelectronic devices is actively pursued.[19–24] Broadly, 2D architectures from organic precursors/polymers are achieved using the following well-established approaches: (i) crystallization-driven self-assembly of covalent polymeric systems pioneered by Manners and Winnik[25–29] and more recently adopted by others,[30–36] (ii) linking symmetrical, mostly planar building blocks, with complementary covalent bonds or dynamic-covalent chemistries to obtain covalent-organic frameworks,[37–39] (iii) construction of single molecular thick layers *via* non-planar building blocks with C_3-symmetric functionality for polymerization in two-dimensions,[40–42] and (iv) crystallization of small organic molecules *via* non-covalent interactions.[43–51] Although the non-covalent synthesis or supramolecular polymerization of small molecules provides an alternative, modular approach to obtain 2D architectures,[52] often this approach has resulted in small-area (<1 μm) structures lacking in high crystallinity.[53–63] Thus rationally achieving crystalline, large-area 2D and 1D organization based on the same π-conjugated building block is a formidable challenge. Such a system/process could enable us to harness the advantages offered by both 1D and 2D organizations in a dynamic system.

[a]*Department of Chemistry, Indian Institute of Technology Bombay, Powai, Mumbai – 400076, India. E-mail: chidambark@chem.iitb.ac.in*

[b]*Centre for Computational and Data Science, Indian Institute of Technology Kharagpur, Kharagpur, West Bengal, India. E-mail: skreddy@iitkgp.ac.in*

[c]*Nanoelectronics and Device Physics Lab, School of Physical Sciences, National Institute of Science Education and Research (NISER), OCC of HBNN, Bhubaneshwar, Jatni, Khurdha, Odisha, India. E-mail: satyaprasad@niser.ac.in*

Herein, we present the controlled supramolecular polymerization of thiazolo[5,4-*d*]thiazole (TzTz), a class of thermally stable, electronically active[64–66] and fluorescent molecular systems,[67–70] into both large-area, crystalline 2D hexagons and 1D nanofibers. Our molecular design comprises a central TzTz core appended with an amide motif on either side, which in turn is connected to a 3,4,5-trialkoxyphenyl (gallic) wedge (Fig. 1a). We envisaged that the amide groups and the π-surface would assist in 1D assembly, whereas the gallic wedge bearing *n*-octyl (**TzTz-C8**), *n*-decyl (**TzTz-C10**), *n*-dodecyl (**TzTz-C12**) or *n*-hexadecyl (**TzTz-C16**) will render the assemblies colloidally stable and also aid in tuning the dimensionality (2D to 1D) of the organization *via* van der Waals interactions of the alkyl chains. We shall first discuss the highly ordered 2D organization observed for **TzTz-C8** and then present the systematic tuning of organization to 1D while moving from **TzTz-C8** to **TzTz-C16**. Thereafter, the molecular level insights into the 1D and 2D organization from molecular dynamics simulation and the functional properties of **TzTz-C8** based optoelectronic devices will be discussed.

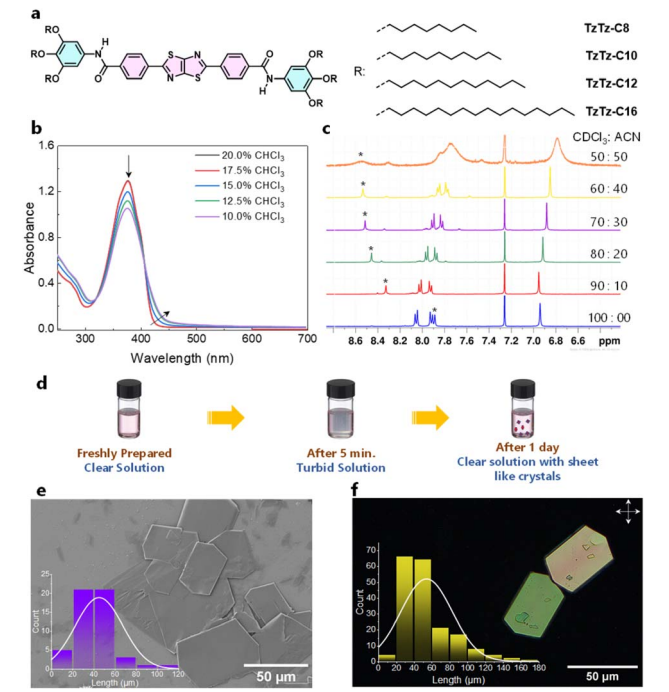

Fig. 1 Self-assembly study of **TzTz-C8**. (a) Molecular structure of the studied TzTz derivatives. (b) UV-vis absorption spectra of **TzTz-C8** in $CHCl_3$: ACN solvent mixtures (v/v, $l = 10$ mm, $c = 20$ μM). The arrows indicate spectral changes with decreasing $CHCl_3$ percentage. (c) Partial ^{1}H-NMR spectra (400 MHz, 298 K) in $CDCl_3$: ACN solvent mixtures (v/v, $c = 3$ mM). * Indicates the amide N–H proton. (d) Schematic representation of the assembly process leading to 2D sheets. (e) Representative FE-SEM image obtained by drop casting the assembled sample on a silicon wafer. The sample was sputtered with 5 nm of gold. (f) Representative polarized optical microscope (POM) image of the sample drop cast on a glass slide and viewed under a cross polarizer. For both (e) and (f), $c = 20$ μM and composition is 10% $CHCl_3$ in ACN. Insets of (e) and (f) show the histograms (analyzed using ImageJ) obtained on various FE-SEM and POM images, respectively.

Results and discussion

Synthesis and bulk properties

The designed TzTz molecules were synthesized by first coupling respective gallic amines and 4-formylbenzoic acid to obtain the aldehyde intermediate containing the amide functionality. This was further condensed with dithiooxamide to obtain the target TzTz molecules (Scheme S1). All the intermediates and final molecules were thoroughly characterized by ^{1}H and ^{13}C NMR spectroscopy and mass spectrometry. First, the bulk properties of TzTz derivatives were characterized by thermogravimetric analysis (TGA), differential scanning calorimetry (DSC) and polarized optical microscopy (POM). The TGA analysis showed <5% weight loss until 350 °C for all the TzTz derivatives, irrespective of the alkyl chain length, indicating their excellent thermal stability (Fig. S1). DSC thermograms showed endothermic melting transitions at 214 °C, 191 °C, 152 °C, and 119 °C for **TzTz-C8**, **TzTz-C10**, **TzTz-C12**, and **TzTz-C16**, respectively (Fig. S2). In addition to the melting and corresponding crystallization, a few other transitions were observed, indicating the potential to form liquid crystalline phases. POM images (viewed under cross-polarizers) of TzTz derivatives cooled from isotropic to room temperature showed birefringence with focal-conic or fan like texture for **TzTz-C8**/**TzTz-C10**/**TzTz-C12** and spherulitic texture for **TzTz-C16** (Fig. S3). The latter suggests the propensity of **TzTz-C16** to form 1D organization.

Controlled solution-phase assembly of TzTz-C8

Next, we studied the solution-phase assembly of **TzTz-C8** using UV-vis absorption and NMR spectroscopy. The UV-vis absorption spectrum of **TzTz-C8** in chloroform ($c = 20$ μM) showed broad absorption from 300–420 nm with a maximum at 380 nm ($\varepsilon_{380\ nm} = 59\,500$ L mol^{-1} cm^{-1}), attributed to the characteristic π–π* transition of the TzTz core (Fig. S4a). A similar spectral profile was observed in other non-polar solvents such as tetrahydrofuran (THF) and toluene, suggesting a molecularly dissolved state in these solvents, whereas, in non-polar methylcyclohexane (MCH), the absorption maximum was blue shifted to 370 nm ($\varepsilon_{370\ nm} = 47\,190$ L mol^{-1} cm^{-1}) and a broad shoulder at around 415 nm was observed (Fig. S4a). To investigate whether these spectral changes are due to intermolecular aggregation in MCH, we carried out concentration-dependent studies. In the concentration range of 50–300 μM, the absorption spectra scaled linearly with the concentration (following Beer–Lambert's law), suggesting the lack of aggregation even in MCH (Fig. S4b and S4c). Although fluorescence spectra can provide insights into the aggregation of chromophores, **TzTz-C8** was found to be non-emissive in the studied solvents ($CHCl_3$, THF, toluene and MCH). On the other hand, in polar solvents (methanol and acetonitrile) **TzTz-C8** was found to be insoluble even at micromolar concentrations. Thus, we studied the assembly behaviour in a mixture of chloroform and acetonitrile (ACN). UV-vis absorption spectra ($c = 20$ μM) of **TzTz-C8** showed no changes when changing the composition from pure $CHCl_3$ to 20% $CHCl_3$ in ACN. However, on further decreasing the volume fraction of $CHCl_3$ to 10%, a gradual drop in absorbance at

380 nm, tailing of the low energy transition until 450 nm and an isosbestic point at 407 nm were observed (Fig. 1b), suggesting intermolecular interaction. To confirm this, composition-dependent ^{1}H-NMR studies were performed. The ^{1}H-NMR chemical shift of amide N–H protons in pure $CDCl_3$ (c = 3 mM) was at 7.88 ppm. On increasing the fraction of polar ACN to 10%, the N–H proton downfield shifted to 8.32 ppm (Fig. 1c). This could be due to a combination of two factors: (i) a steep increase in the polarity of the composition and (ii) intermolecular hydrogen bonding. On further gradual increase of the ACN fraction to 50% (in steps of 10%), a gradual downfield shift of N–H protons to 8.53 ppm and broadening were observed. The gradual downfield shift of N–H protons beyond 10% ACN suggests that the sharp downfield shift ($\Delta\delta$ = 0.44 ppm) at 10% ACN composition was largely due to the sudden change in solvent polarity from pure $CDCl_3$ to 10% ACN in $CDCl_3$. Also, with the increase in the fraction of ACN, the aromatic protons of the core and gallic wedge undergo an upfield shift and broadening, clearly indicating the presence of intermolecular hydrogen bonding in a mixture of $CHCl_3$ and ACN.

Interestingly, a freshly prepared sample of **TzTz-C8** in 10% $CHCl_3$ in ACN (c = 20 μM) was a clear solution. However, after 5 min of standing at room temperature (25–35 °C) it became turbid, indicating the potential assembly of the system. After 24 hours at room temperature (undisturbed), lustrous crystals visible to the naked eye were observed at the bottom of the vial (Fig. 1d). These crystals were transferred onto a suitable substrate and analyzed by field emission scanning electron microscopy (FE-SEM) and POM. FE-SEM micrographs showed micron-sized, hexagonal morphology with varied lateral dimensions (Fig. 1e and S5). Similar micron-sized structures with birefringence were observed using POM under cross-polarizers (Fig. 1f and S6), indicating the highly anisotropic arrangement of molecules in the hexagonal-shaped structures. The analysis of many such structures from FE-SEM and POM micrographs indicates that the typical long-axis of the hexagon (defined as length) is 40–50 μm (inset of Fig. 1e and f). The thickness of these hexagonal crystals as measured by atomic force microscopy (AFM) height analysis and a stylus profilometer was in the range of 100–500 nm (Fig. S7 and S8), indicating multiple layers of sheets stacked on top of each other. To understand if the sheets are in a metastable or kinetically trapped state, a freshly prepared sample was heated to the molecularly dissolved state and cooled to room temperature at a controlled rate (2 °C min^{-1}). The resultant sheets (after 12 hours) were highly birefringent and hexagonal (Fig. S9), suggesting the negligible role of sample preparation in obtaining such large-area sheets. Also, studies in dry 10% $CHCl_3$ in ACN (c = 20 μM) resulted in large-area sheets (Fig. S10), suggesting the negligible role of residual water in influencing the sheet formation. Furthermore, it is worth noting that the lateral dimensions observed in **TzTz-C8** are significantly larger (>10 μm) than those observed for previously reported self-assembled small molecules (<1 μm).[53,60,61]

To understand the formation of large-area sheets, time-dependent steady-state UV-vis spectroscopy and microscopic analysis were carried out on **TzTz-C8** (c = 20 μM, 10% $CHCl_3$ in ACN). The time-dependent UV-vis spectral profile shows a minor decrease in absorbance up to 8 hours and thereafter a significant drop in absorbance was observed (Fig. S11). For microscopic analysis, aliquots of freshly prepared samples were drop-cast on a suitable substrate and analyzed by FE-SEM and POM at different intervals of time. It can be observed that until 8 hours slightly birefringent and ill-defined hexagons were formed (Fig. S12). However, the samples equilibrated for 12 hours and beyond at room temperature (25–30 °C) showed clear birefringent sheets in POM and well-defined hexagonal morphology in FE-SEM (Fig. S12). This suggests that at least 12 hours at room temperature (25–30 °C) are required to achieve well-defined sheets. However, as can be seen from the length histogram (inset of Fig. 1e and f), sheets of varied lengths (or high dispersity) are formed. In order to obtain sheets with controlled length distribution, the 10% $CHCl_3$ in ACN solution after 12 hours was carefully decanted to separate the apparently clear top layer and the bottom containing visibly large crystals. Imaging the supernatant showed sheets of 40–60 μm in length, whereas the crystals at the bottom were significantly large (hundreds of microns in length) (Fig. S13). This suggests that a non-covalent synthetic approach using the differential densities of the sheets could be employed to obtain sheets of markedly different lengths.

Next, we explored the assembly of **TzTz-C8** in various solvent compositions and concentrations to explore the generality of large-area sheet formation. First, we varied the concentration (10–50 μM) and composition of $CHCl_3$ (10–50%) in ACN. The concentration-composition phase diagram shows that for 20–50 μM and 10–20% $CHCl_3$ in ACN, large-area sheets are observed (Fig. 2a). However, at a higher percentage of solvent (30–50% $CHCl_3$), as expected, no assembly was observed (Fig. 2a). To explore the versatility of sheet formation, various solvent mixtures were investigated. Notably, similar large-area,

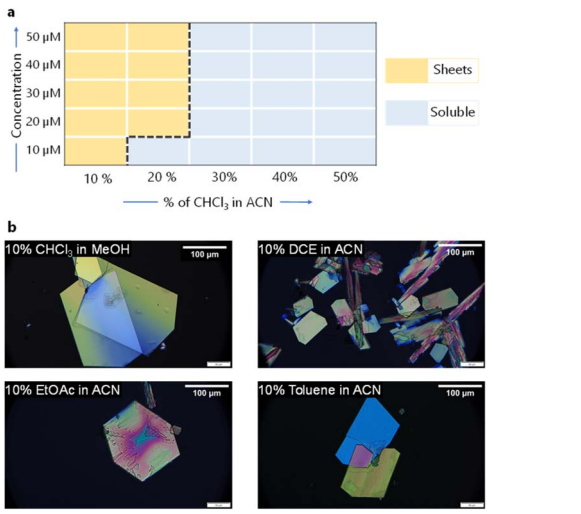

Fig. 2 (a) Concentration-composition phase diagram of TzTz-C8 showing the conditions under which sheets are observed. (b) Representative POM image (under cross-polarizers) of the large-area 2D sheets observed in different solvent combinations (c = 40 μM).

birefringent, hexagonal morphology was observed using different solvent combinations, such as methanol/$CHCl_3$, 1,2-dichloroethane/ACN, ethyl acetate/ACN, and toluene/ACN (c = 40 μM, Fig. 2b and S14). In these mixtures, $CHCl_3$, 1,2-dichloroethane, ethyl acetate, and toluene served as solvents, promoting molecular dissolution, whereas MeOH and ACN acted as anti-solvents, inducing assembly. This further reinforces that large-area sheets are observed when the right balance between solubility and aggregation is achieved, irrespective of the concentration and composition.

Influence of alkyl chain length on dimensionality of supramolecular polymers

To understand the molecular level origin of the high crystallinity in **TzTz-C8**, we studied other TzTz derivatives with variation in alkyl chain length (**TzTz-C10**, **TzTz-C12**, and **TzTz-C16**) on the gallic wedge. UV-vis absorption and ^{1}H-NMR spectroscopic studies suggest that **TzTz-C10** and **TzTz-C12** assemble in $CHCl_3$: ACN solvent composition *via* intermolecular hydrogen bonding, analogous to that observed for **TzTz-C8** (Fig. S15 and S16). The time-dependent UV-vis spectral profile of **TzTz-C10** showed a gradual drop in absorbance with saturation around 6 hours (Fig. S17). Similarly, time evolution of morphology studied by FE-SEM (c = 10 μM, 10% $CHCl_3$ in ACN) showed no mesoscopic ordering until 2 hours; however at and beyond 4 hours elongated structures were observed (Fig. 3a and S18), suggesting the sluggish growth kinetics of **TzTz-C10**, analogous to **TzTz-C8**. On the other hand, the time-dependent UV-vis spectral profile (c = 10 μM, 30% $CHCl_3$ in ACN) of **TzTz-C12** saturated within 10 minutes (Fig. S19). Also, time resolved FE-SEM studies showed that only 2D structures are formed until 5 minutes after sample preparation. At 10 minutes and beyond 1D nanofibers were observed, in addition to few 2D sheets (Fig. 3b and S20). Intriguingly, for a fully equilibrated (after 30 minutes) **TzTz-C12** solution (c = 10 μM, 30% $CHCl_3$ in ACN), the supernatant and the material settled at the bottom of the vials showed exclusively 2D sheets and 1D nanofibers, respectively, thus providing access to both 1D and 2D morphologies from the same building block (Fig. 3c and S21).

Intrigued by the observation of 1D nanofibers in **TzTz-C12**, we further studied **TzTz-C16** bearing longer alkyl chains. The UV-vis spectra (c = 10 μM) of **TzTz-C16** showed a gradual decrease in absorbance and a hypsochromic shift of λ_{max} by 17 nm (to 364 nm) as the solvent composition was varied from pure $CHCl_3$ to 60% $CHCl_3$ in ACN (Fig. 4a). This is in contrast to the UV-vis spectral features observed for other TzTz derivatives in which only a decrease in absorbance was noted (Fig. 1b). The hypsochromic shift suggests a change in packing to H-type of aggregate for **TzTz-C16**. Concentration-dependent ^{1}H-NMR

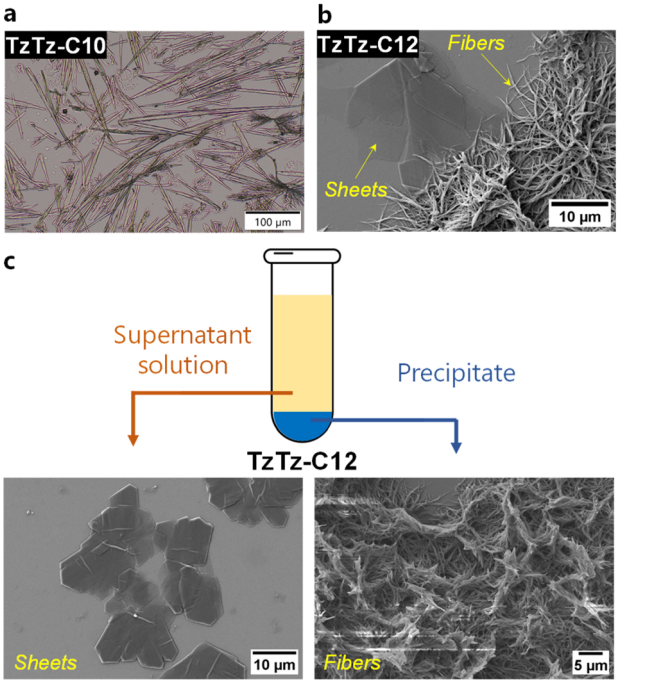

Fig. 3 Morphological studies of **TzTz-C10** and **TzTz-C12**. (a) and (b) Representative optical and FE-SEM micrographs of **TzTz-C10** (c = 10 μM, 10% $CHCl_3$ in ACN) and **TzTz-C12** (c = 10 μM, 30% $CHCl_3$ in ACN), respectively, obtained by drop casting assembled samples on a silicon wafer. The sample was sputtered with 5 nm of gold. (c) FE-SEM micrographs of **TzTz-C12** (c = 10 μM, 30% $CHCl_3$ in ACN) obtained by drop casting of supernatant solution and precipitation on a silicon wafer.

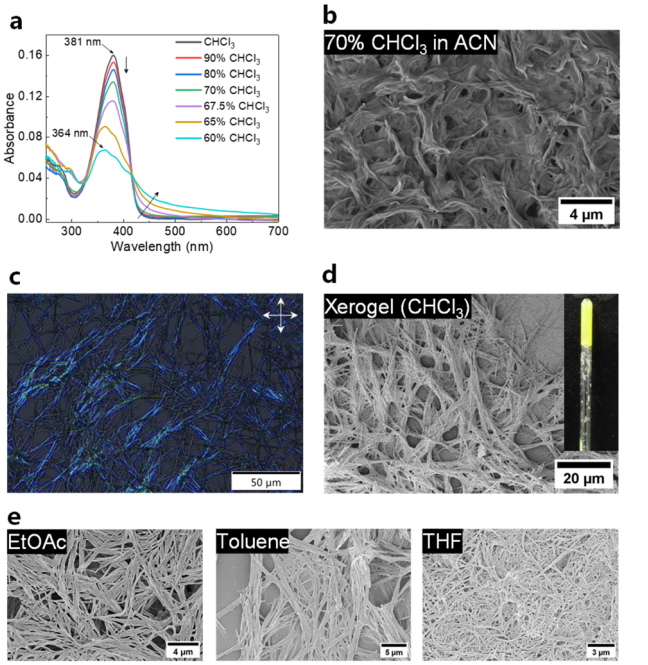

Fig. 4 Self-assembly study of **TzTz-C16**. (a) UV-vis absorption spectra of **TzTz-C16** in an ACN/$CHCl_3$ solvent mixture (v/v, c = 10 μM, l = 2 mm). The arrows indicate spectral changes with decreasing $CHCl_3$ percentage. (b) FE-SEM micrograph obtained by drop casting the assembled sample (c = 10 μM, 70% $CHCl_3$ in ACN) on a silicon wafer. The sample was sputtered with 5 nm of gold. (c) POM and (d) FE-SEM micrograph of a xerogel obtained from a $CHCl_3$ (c = 3.5 mM, $CHCl_3$) solution of **TzTz-C16** drop cast on a glass slide (viewed under a cross polarizer) and silicon wafer, respectively. (e) FE-SEM micrographs of **TzTz-C16** assembled in different solvents: toluene (c = 500 μM), THF (c = 500 μM), and EtOAc (c = 250 μM).

studies in $CDCl_3$ confirmed the presence of intermolecular hydrogen bonding for **TzTz-C16** (Fig. S22). The time-dependent UV-vis spectral profile showed full equilibration within 30 min (Fig. S23), suggesting the rapid kinetics involved in the system. Furthermore, time-resolved FE-SEM studies showed exclusively high aspect ratio 1D nanofibers formed within 30 minutes (Fig. 4b and S24). Remarkably, the 1D nanofibers formed a weak gel (which becomes a partly flowing semi-solid on prolonged standing at room temperature) in $CDCl_3$ (Fig. 4c, d and S25), and also the 1D morphology was observed in solvents of different polarities (Fig. 4e), suggesting that the packing is independent of the solvent polarity.

The marked differences in UV-vis spectral features and morphology between the different TzTz derivatives indicate that alkyl chain length on the gallic wedge plays a significant role in dictating the molecular packing. To study ordering in these morphologies, X-ray diffraction (XRD) patterns of the assembled structures were recorded. The XRD of **TzTz-C8** sheets formed from $CHCl_3$: ACN composition showed prominent and sharp diffraction peaks with the principal peak (q^*) at 5.71°, followed by 2θ values of 11.17° ($\sqrt{4}q^*$) and 22.42° ($\sim\sqrt{9}q^*$), corresponding to interplanar distances of 15.46 Å, 7.92 Å, and 3.96 Å, respectively (Fig. 5). Such an XRD pattern with q^*, $\sqrt{4}q^*$ and $\sqrt{9}q^*$ relationship between the first three high intensity reflections suggests the presence of a highly ordered lamellar arrangement of molecules in the sheets.[71] In addition to the sharp signals corresponding to the lamellar ordering, few low intensity peaks were also observed, which prohibited the full single crystal structural analysis to obtain the exact molecular arrangement. A similar XRD pattern was observed in other solvent mixtures such as $CHCl_3$/methanol (Fig. S26), indicating lamellar packing. On the other hand, XRD of drop-cast (from the as-synthesized) **TzTz-C8** showed a broad peak around 20° (2θ), suggesting the amorphous nature of the sample (Fig. S27).

The XRD pattern of **TzTz-C10** exhibits multiple sharp reflections, with a prominent low angle peak at 3.65°. This hints towards a structure with at least one of the dimensions being elongated, which is in-line with the elongated 2D structures observed in FE-SEM. The XRD of as-synthesized sample **TzTz-C10** showed a broad peak at 20° indicating the amorphous nature of the sample (Fig. S28), analogous to that observed in **TzTz-C8**. The XRD pattern of self-assembled **TzTz-C12** was significantly broader and, interestingly, the reflections observed for **TzTz-C8** were also present in **TzTz-C12** (5.87°, 11.18° and 23.12°), in addition to other reflections. This again confirms the presence of 2D sheets in **TzTz-C12** along with 1D nanofibers, as observed from FE-SEM micrographs (Fig. 3c). Finally, the XRD pattern of self-assembled **TzTz-C16** was significantly broad with a prominent peak at 23.35° (3.80 Å), corresponding to π-stacking distance.[72,73] This is in agreement with the hypsochromic shift observed in UV-vis spectra due to strong interaction between the π-surfaces. Thus, the solution-phase assembly plays a paramount role in obtaining highly crystalline, large-area sheets and 1D nanofibers with the length of the alkyl chains playing a pivotal role.

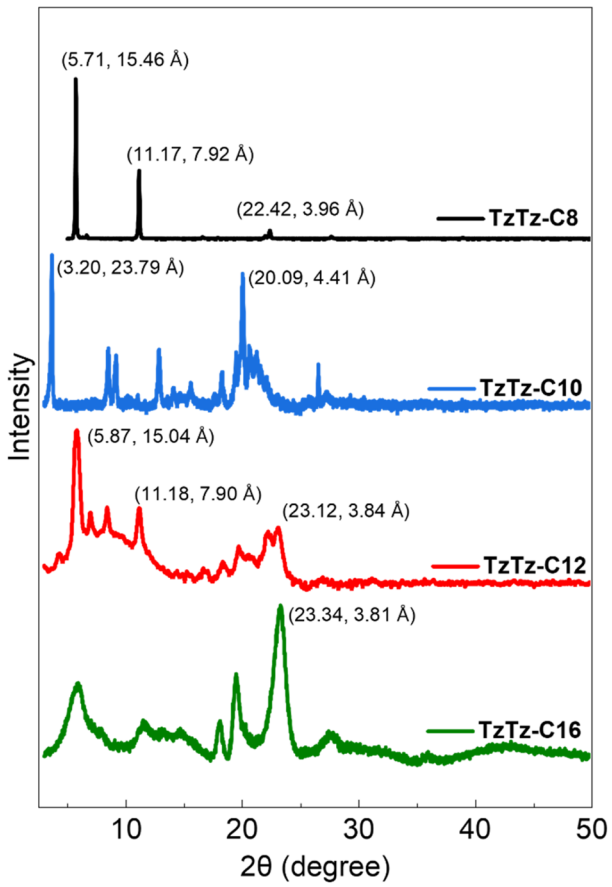

Fig. 5 X-ray diffraction pattern of the assembled TzTz derivatives from $CHCl_3$: ACN composition.

Molecular dynamics simulations

Classical molecular dynamics (MD) simulations were conducted to investigate the molecular packing and the structural evolution of both **TzTz-C8** and **TzTz-C16** nanofibers. ^{1}H-NMR analysis confirmed the presence of intermolecular hydrogen bonds between amide groups in both TzTz derivative assemblies. Thus, for the MD simulations, 1D nanofibers comprising 30 monomeric units of **TzTz-C8** and **TzTz-C16** with intermolecular hydrogen bonding were constructed (Fig. S29 and S30). MD trajectory analysis reveals that both nanofiber assemblies show dynamic behaviour during the simulation timescale (100 ns). The structural evolution of assemblies was characterized using contact maps of all pairs of S, N, and H atoms of the TzTz core of each monomer pair for both nanofibers (Fig. 6a and b and S31). The contact maps revealed a distinct pattern of contacts between non-adjacent molecules. This pattern is more pronounced in **TzTz-C8** nanofibers, where frequent interactions between the non-adjacent molecules are observed (off-diagonal elements in the contact map, Fig. 6a), whereas in **TzTz-C16** interactions are largely with the neighbouring monomers (exhibiting a tridiagonal matrix pattern). This suggests that **TzTz-C8** nanofiber displays more flexibility and bending compared to **TzTz-C16**, which, in turn, causes the non-adjacent molecules in **TzTz-C8** to interact laterally, forming motifs

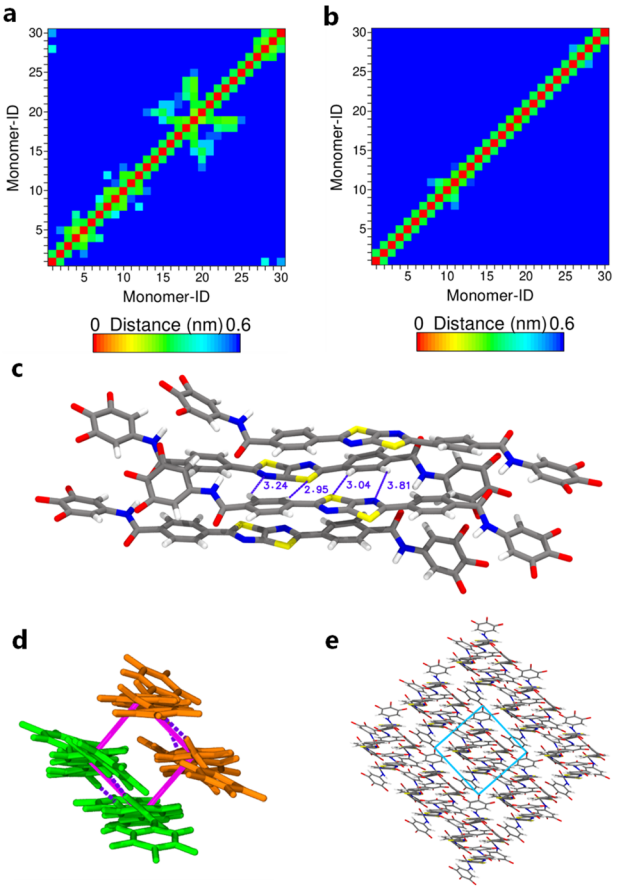

Fig. 6 Molecular dynamics simulations. (a) and (b) Contact maps depicting short contacts between the peripheral atoms (S, N, and H) of the TzTz cores of 30 monomers of **TzTz-C8** and **TzTz-C16**, respectively. (c) Representative arrangement of four **TzTz-C8** monomers observed during the MD simulations. Lateral C–H···S and C–H···N hydrogen bonds are observed between non-adjacent molecules in **TzTz-C8**. (d) The side-view of the four **TzTz-C8** monomers exhibiting a brickwork-like motif. Each pair of monomers (shown with the same color) is stabilized by intermolecular hydrogen bonding (dashed lines). (e) Representative extended 2D arrangement based on calculated approximate lattice parameters of the 2D unit cell being 14 Å and 9 Å (twice the lattice vector length shown in (d)). The alkyl side chains are not shown for clarity. Color codes used in (c): carbon in grey; hydrogen in white; nitrogen in blue; oxygen in red; sulphur in yellow.

similar to those found in 2D sheet-like structures. The hydrogen-bonding network between amide groups of neighbouring molecules remained stable throughout simulations, consistent with ^{1}H-NMR experimental observations. The alkyl side-chains show pronounced dynamic behaviour, characterized by intermolecular twinning and transient interactions among neighbouring side chains, resulting in a somewhat disordered arrangement. In **TzTz-C16**, the long side chains display stronger chain–chain van der Waals interactions. However, at the same time, steric congestions due to the longer alkyl chains prevent lateral interactions between peripheral atoms of the TzTz core. Furthermore, terminal monomers of the **TzTz-C8** nanofibers also showed close contact with adjacent molecules during the simulations. This suggests that in the case of **TzTz-C8**, initially 1D nanofibers form; however, due to the increased lateral interaction between the monomers, they fold and adopt a brickwork-like arrangement within the contact regions. This is illustrated in Fig. 6c, which shows the arrangement of four **TzTz-C8** monomers observed during the MD simulations. The lateral contacts mediated by weaker C–H···S and C–H···N hydrogen bonding interactions stabilize this arrangement, as shown in Fig. 6c, d and S32. This observation is consistent with the X-ray diffraction (XRD) pattern, which indicates a highly ordered lamellar arrangement for **TzTz-C8**. Moreover, the FE-SEM and POM micrographs reveal a hexagonal morphology that is characteristic of a brickwork-like arrangement of molecular units, as observed in the simulations.

Based on the observed arrangement of the four **TzTz-C8** monomers in the MD simulations, the approximate lattice parameters of the 2D unit cell are calculated to be 14 Å and 9 Å (Fig. 6e), which is in close agreement with the experimental lamellar *d*-spacing of 15.6 Å. The core–core radial distribution functions ($g(r)$) corresponding to the **TzTz-C8** and **TzTz-C16** nanofibers (Fig. S33) indicate a higher degree of stacking order between monomer units in **TzTz-C16** compared to **TzTz-C8**. This observation aligns with the experimentally observed hypsochromic shift of UV-vis spectra of **TzTz-C16**, suggesting stronger interactions between neighbouring **TzTz-C16** molecules.

Electrical conductivity of TzTz-C8

The observation of solution-phase grown micron-sized 2D morphology in a system with an electronically active core (**TzTz-C8**) motivated us to further explore the electrical properties of this system. We utilized a custom-designed hollow chamber (2 mL) which was securely attached using silicone adhesive over a patterned Cr/Au electrode channel fabricated on glass

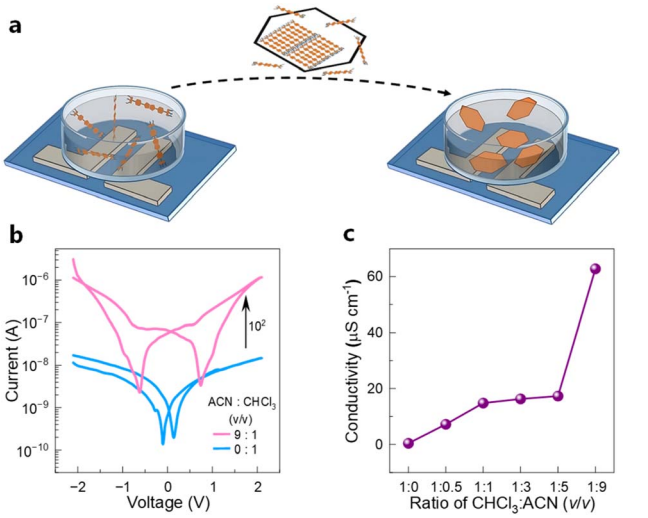

Fig. 7 Electrical characterization of **TzTz-C8**. (a) Device schematic for the conductivity measurements. (b) Comparison of *I*–*V* sweep between **TzTz-C8** in pure $CHCl_3$ and in 10% $CHCl_3$ in ACN. (c) Comparison of conductivity on increasing the ratio of ACN in the mixture.

substrates (Fig. 7a) for this purpose. A solution of **TzTz-C8** (c = 20 μM) in $CHCl_3$ was first poured into the chamber and I–V characteristics were measured over a voltage range of −2 V to +2 V (Fig. 7b). The voltage range was chosen so that it is within the electrochemical window of the solvent used and artefacts from electrochemical modification of the solvents do not contribute to the observed channel current. Devices fabricated from the pristine $CHCl_3$ phase exhibited a rather low channel current of ∼10–20 nA. Upon incorporation of acetonitrile into the chamber we observed an increase in the conductivity (Fig. 7b and S34). The channel current increases and reaches a maximum value of ∼1 μA for 10% $CHCl_3$ in ACN composition, consistent with the microscopic studies in which birefringent hexagonal sheets were observed. Consequently, the conductivity reaches a maximum value of ∼63 μS cm^{-1} (Fig. 7c). Typical fits for conductivity measurements are shown in Fig. S35. This behaviour of the increase in channel current and the overall conductivity with the increasing volume fraction of ACN can thus be attributed to the enhancement in crystallinity of the resultant assembled structure. From Fig. 7c we observe that the composition with maximum channel current (10% $CHCl_3$ in ACN) coincides with the composition at which formation of ordered 2D hexagonal structures is seen, thus suggesting that improved molecular ordering leads to higher channel currents. Interestingly, when the temporal evolution of the conductivity of the solution was monitored, we observed that the conductivity increases until 10 h (Fig. S34b). This is in-line with the 8–10 hours required to form equilibrated 2D hexagons of **TzTz-C8**, as observed from solution state kinetics. Our measurements provide important insights through sensitive conductometric measurement of the solvent induced crystallization/self-assembly processes in this class of semiconductors.

Conclusions

In summary, we have shown that in the family of TzTz based amides both micron-sized 2D sheets and 1D nanofibers can be obtained by tuning the van der Waals interactions of the peripheral alkyl chains. XRD studies on assembled structures and molecular dynamics simulations together indicate that in **TzTz-C8**, due to shorter alkyl chain length, side-on brickwork like packing mediated by the C–H···S and C–H···N interactions is observed. However, with the longer *n*-hexadecyl alkyl chain derivative (**TzTz-C16**), the van der Waals interactions in a 1D nanofiber are stronger leading to 1D morphology. Intriguingly, for an intermediate alkyl chain length (**TzTz-C12**), both 2D sheets and 1D nanofibers are observed. This represents a unique non-covalent synthetic methodology to achieve more than one kind of nanostructure from the same system. Furthermore, the temporal evolution of 2D sheets was observed by *in situ* electrical conductivity measurements, indicating the potential application of such systems. These findings highlight that even with a classical monomer design (hydrogen bonding units on either side of a linear π-conjugated core), it is non-trivial to foresee the morphology of the assembled structure. The subtle competition between the alkyl chain crystallization and the interactions between the π-conjugated core (*via* heteroatoms) dictates the mesoscopic morphology. We envisage that our findings can potentially be applied to a large number of heteroatom bearing π-conjugated systems known in the literature, resulting in exquisite control over the morphology and the resultant electronic properties.

Author contributions

C. K. and A. T. conceived the project. A. T. carried out all the experimental work (synthesis, spectroscopic and microscopic studies). U. P. and D. I. S. carried out the electrical measurements under the supervision of S. P. S. R. S. and S. K. R. carried out MD simulations. C. K. supervised the overall project. A. T. and C. K. wrote the initial draft of the manuscript. All authors discussed the results and contributed to the writing.

Conflicts of interest

There are no conflicts to declare.

Data availability

The data supporting this article have been included as part of the SI. Supplementary information: Materials and methods, synthetic, computational and device fabrication details, supporting figures and tables, spectral copies, and references. See DOI: **https://doi.org/10.1039/d5sc03874j**.

Acknowledgements

C. K. acknowledges funding from the IIT Bombay Seed grant (RD/0520-IRCCSH0-001), DST-INSPIRE faculty fellowship (IFA19-CH316) and Science and Engineering Research Board, Government of India (SRG/2020/002485 and CRG/2023/004212). C. K. and A. T. thank the department of chemistry, IIT Bombay, and Institute of Eminence (IoE) for various facilities. A. T. and C. K. thank Mr Rajesh Gunjal for assistance with MALDI-TOF experiments. C. K. and A. T. thank Satyabrata Behera and Sourav Nandi for useful comments on the manuscript. S. K. R. acknowledges the Core Research grant (SERB-CRG) from the Science and Engineering Research Board (grant number CRG/2022/006457) for financial support. This work also used the computing resources of 'PARAM Shakti' at IIT Kharagpur which is a part of the National Supercomputing Mission (NSM), which is implemented by C-DAC and supported by the Ministry of Electronics and Information Technology (MeitY) and Department of Science and Technology (DST), Government of India. R. S. thanks UGC, India, for a Senior Research Fellowship. SPS acknowledges funding support from DAE, Government of India, for funding to NISER, Bhubaneswar, through project RIN-4001, and SERB for funding through IPA/2021/000096. UP and DIS acknowledge DAE, Government of India, for a fellowship.

Notes and references

1 T. Aida, E. W. Meijer and S. I. Stupp, *Science*, 2012, **335**, 813–817.

2 H.-Q. Peng, W. Zhu, W.-J. Guo, Q. Li, S. Ma, C. Bucher, B. Liu, X. Ji, F. Huang and J. L. Sessler, *Prog. Polym. Sci.*, 2023, **137**, 101635.
3 P. K. Hashim, J. Bergueiro, E. W. Meijer and T. Aida, *Prog. Polym. Sci.*, 2020, **105**, 101250.
4 L. Yang, X. Tan, Z. Wang and X. Zhang, *Chem. Rev.*, 2015, **115**, 7196–7239.
5 T. D. Clemons and S. I. Stupp, *Prog. Polym. Sci.*, 2020, **111**, 101310.
6 T. F. A. De Greef, M. M. J. Smulders, M. Wolffs, A. P. H. J. Schenning, R. P. Sijbesma and E. W. Meijer, *Chem. Rev.*, 2009, **109**, 5687–5754.
7 D. Zhao and J. S. Moore, *Org. Biomol. Chem.*, 2003, **1**, 3471–3491.
8 C. Kulkarni, S. Balasubramanian and S. J. George, *ChemPhysChem*, 2013, **14**, 661–673.
9 Z. Chen, A. Lohr, C. R. Saha-Möller and F. Würthner, *Chem. Soc. Rev.*, 2009, **38**, 564–584.
10 D. van der Zwaag, T. F. A. de Greef and E. W. Meijer, *Angew. Chem., Int. Ed.*, 2015, **54**, 8334–8336.
11 S. Ogi, T. Fukui, M. L. Jue, M. Takeuchi and K. Sugiyasu, *Angew. Chem., Int. Ed.*, 2014, **53**, 14363–14367.
12 M. Wehner and F. Würthner, *Nat. Rev. Chem.*, 2019, **4**, 38–53.
13 J. Matern, Y. Dorca, L. Sánchez and G. Fernández, *Angew. Chem., Int. Ed.*, 2019, **58**, 16730–16740.
14 P. A. Korevaar, S. J. George, A. J. Markvoort, M. M. J. Smulders, P. A. J. Hilbers, A. P. H. J. Schenning, T. F. A. De Greef and E. W. Meijer, *Nature*, 2012, **481**, 492–496.
15 L. Borsdorf, L. Herkert, N. Bäumer, L. Rubert, B. Soberats, P. A. Korevaar, C. Bourque, C. Gatsogiannis and G. Fernández, *J. Am. Chem. Soc.*, 2023, **145**, 8882–8895.
16 S. Ogi, K. Sugiyasu, S. Manna, S. Samitsu and M. Takeuchi, *Nat. Chem.*, 2014, **6**, 188–195.
17 S. Ogi, V. Stepanenko, K. Sugiyasu, M. Takeuchi and F. Würthner, *J. Am. Chem. Soc.*, 2015, **137**, 3300–3307.
18 F. García, R. Gómez and L. Sánchez, *Chem. Soc. Rev.*, 2023, **52**, 7524–7548.
19 S. I. Stupp, S. Son, H. C. Lin and L. S. Li, *Science*, 1993, **259**, 59–63.
20 P. Miró, M. Audiffred and T. Heine, *Chem. Soc. Rev.*, 2014, **43**, 6537–6554.
21 T. Kim, J. Y. Park, J. Hwang, G. Seo and Y. Kim, *Adv. Mater.*, 2020, **32**, 2002405.
22 Y. Ren and Y. Xu, *Chem. Soc. Rev.*, 2024, **53**, 1823–1869.
23 M. Gobbi, E. Orgiu and P. Samorì, *Adv. Mater.*, 2018, **30**, 1706103.
24 B. Shen, Y. Kim and M. Lee, *Adv. Mater.*, 2020, **32**, 1905669.
25 C. E. Boott, A. Nazemi and I. Manners, *Angew. Chem., Int. Ed.*, 2015, **54**, 13876–13894.
26 X. He, Y. He, M. S. Hsiao, R. L. Harniman, S. Pearce, M. A. Winnik and I. Manners, *J. Am. Chem. Soc.*, 2017, **139**, 9221–9228.
27 R. Deng, X. Mao, S. Pearce, J. Tian, Y. Zhang and I. Manners, *J. Am. Chem. Soc.*, 2022, **144**, 19051–19059.
28 Z. M. Hudson, C. E. Boott, M. E. Robinson, P. A. Rupar, M. A. Winnik and I. Manners, *Nat. Chem.*, 2014, **6**, 893–898.
29 X. He, M.-S. Hsiao, C. E. Boott, R. L. Harniman, A. Nazemi, X. Li, M. A. Winnik and I. Manners, *Nat. Mater.*, 2017, **16**, 481–488.
30 S. Yang, S. Shin, I. Choi, J. Lee and T. L. Choi, *J. Am. Chem. Soc.*, 2017, **139**, 3082–3088.
31 S. Yang, S. Y. Kang and T. L. Choi, *J. Am. Chem. Soc.*, 2019, **141**, 19138–19143.
32 S. Park, S. Y. Kang, S. Yang and T. L. Choi, *J. Am. Chem. Soc.*, 2024, **146**, 19369–19376.
33 M. Inam, J. R. Jones, M. M. Pérez-Madrigal, M. C. Arno, A. P. Dove and R. K. O'Reilly, *ACS Cent. Sci.*, 2018, **4**, 63–70.
34 T. Xia, L. Xiao, K. Sun, J. Y. Rho, Y. Xie, S. J. Parkinson, L. Sangroniz, J. Zhang, J. Lin, A. J. Müller, L. Gao, A. P. Dove and R. K. O'Reilly, *Macromolecules*, 2024, **57**, 11210–11220.
35 A. Rajak and A. Das, *Angew. Chem., Int. Ed.*, 2022, **61**, e202116572.
36 A. D. Merg, E. Van Genderen, A. Bazrafshan, H. Su, X. Zuo, G. Touponse, T. B. Blum, K. Salaita, J. P. Abrahams and V. P. Conticello, *J. Am. Chem. Soc.*, 2019, **141**, 20107–20117.
37 J. W. Colson and W. R. Dichtel, *Nat. Chem.*, 2013, **5**, 453–465.
38 S. Kandambeth, K. Dey and R. Banerjee, *J. Am. Chem. Soc.*, 2019, **141**, 1807–1822.
39 S. Kandambeth, A. Mallick, B. Lukose, M. V. Mane, T. Heine and R. Banerjee, *J. Am. Chem. Soc.*, 2012, **134**, 19524–19527.
40 J. Sakamoto, J. Van Heijst, O. Lukin and A. D. Schlüter, *Angew. Chem., Int. Ed.*, 2009, **48**, 1030–1069.
41 M. J. Kory, M. Wörle, T. Weber, P. Payamyar, S. W. Van De Poll, J. Dshemuchadse, N. Trapp and A. D. Schlüter, *Nat. Chem.*, 2014, **6**, 779–784.
42 P. Kissel, D. J. Murray, W. J. Wulftange, V. J. Catalano and B. T. King, *Nat. Chem.*, 2014, **6**, 774–778.
43 C. Liao, Y. Gong, Y. Che, H. Ji, B. Liu, L. Zang, Y. Che and J. Zhao, *Nat. Commun.*, 2024, **15**, 5668.
44 Y. Gong, C. Cheng, H. Ji, Y. Che, L. Zang, J. Zhao and Y. Zhang, *J. Am. Chem. Soc.*, 2022, **144**, 15403–15410.
45 J. F. Woods, L. Gallego, A. Maisch, D. Renggli, C. Cuocci, O. Blacque, G. Steinfeld, A. Kaech, B. Spingler, A. Vargas Jentzsch and M. Rickhaus, *Nat. Commun.*, 2023, **14**, 4725.
46 L. Gallego, J. F. Woods and M. Rickhaus, *Org. Mater.*, 2022, **4**, 137–145.
47 C. He, D. Wu, F. Zhang, M. Xue, X. Zhuang, F. Qiu and X. Feng, *ChemPhysChem*, 2013, **14**, 2954–2960.
48 N. Seiki, Y. Shoji, T. Kajitani, F. Ishiwari, A. Kosaka, T. Hikima, M. Takata, T. Someya and T. Fukushima, *Science*, 2015, **348**, 1122–1126.
49 Y. X. Li, X. M. Dong, M. N. Yu, W. Liu, Y. J. Nie, J. Zhang, L. H. Xie, C. X. Xu, J. Q. Liu and W. Huang, *Small*, 2021, **17**, 2102060.
50 M. Ghora, P. Majumdar, M. Anas and S. Varghese, *Chem.–Eur. J.*, 2020, **26**, 14488–14495.
51 L. Meazza, J. A. Foster, K. Fucke, P. Metrangolo, G. Resnati and J. W. Steed, *Nat. Chem.*, 2013, **5**, 42–47.
52 I. Insua and J. Montenegro, *J. Am. Chem. Soc.*, 2020, **142**, 300–307.
53 C. M. Atienza and L. Sánchez, *Chem.–Eur. J.*, 2024, **30**, e202400379.

54 Z. Jin, N. Sasaki, N. Kishida, M. Takeuchi, Y. Wakayama and K. Sugiyasu, *Chem.–Eur. J.*, 2023, **29**, e202302181.
55 S. Dhiman, R. Ghosh, S. Sarkar and S. J. George, *Chem. Sci.*, 2020, **11**, 12701–12709.
56 M. Vybornyi, A. Rudnev and R. Häner, *Chem. Mater.*, 2015, **27**, 1426–1431.
57 Z. Chen, M. H. Y. Chan and V. W. W. Yam, *J. Am. Chem. Soc.*, 2020, **142**, 16471–16478.
58 S. Chen, S. M. Polen, L. Wang, M. Yamasaki, C. M. Hadad and J. D. Badjić, *J. Am. Chem. Soc.*, 2016, **138**, 11312–11317.
59 I. Insua, J. Bergueiro, A. Méndez-Ardoy, I. Lostalé-Seijo and J. Montenegro, *Chem. Sci.*, 2022, **13**, 3057–3068.
60 N. Sasaki, J. Kikkawa, Y. Ishii, T. Uchihashi, H. Imamura, M. Takeuchi and K. Sugiyasu, *Nat. Chem.*, 2023, **15**, 922–929.
61 T. Fukui, S. Kawai, S. Fujinuma, Y. Matsushita, T. Yasuda, T. Sakurai, S. Seki, M. Takeuchi and K. Sugiyasu, *Nat. Chem.*, 2017, **9**, 493–499.
62 C. A. Shen, D. Bialas, M. Hecht, V. Stepanenko, K. Sugiyasu and F. Würthner, *Angew. Chem., Int. Ed.*, 2021, **60**, 11949–11958.
63 T. Schnitzer, B. W. L. van den Bersselaar, B. A. G. Lamers, M. H. C. van Son, S. J. D. Maessen, F. V. de Graaf, B. F. M. de Waal, N. Trapp, G. Vantomme and E. W. Meijer, *J. Am. Chem. Soc.*, 2025, **147**, 1991–1999.
64 I. Osaka, R. Zhang, G. Sauvè, D. M. Smilgies, T. Kowalewski and R. D. McCullough, *J. Am. Chem. Soc.*, 2009, **131**, 2521–2529.
65 I. Osaka, G. Sauvé, R. Zhang, T. Kowalewski and R. D. McCullough, *Adv. Mater.*, 2007, **19**, 4160–4165.
66 S. Ando, J.-I. Nishida, H. Tada, Y. Inoue, S. Tokito and Y. Yamashita, *J. Am. Chem. Soc.*, 2005, **127**, 5336–5337.
67 I. Roy, S. Bobbala, J. Zhou, M. T. Nguyen, S. K. M. Nalluri, Y. Wu, D. P. Ferris, E. A. Scott, M. R. Wasielewski and J. F. Stoddart, *J. Am. Chem. Soc.*, 2018, **140**, 7206–7212.
68 A. N. Woodward, J. M. Kolesar, S. R. Hall, N. A. Saleh, D. S. Jones and M. G. Walter, *J. Am. Chem. Soc.*, 2017, **139**, 8467–8473.
69 N. A. Sayresmith, A. Saminathan, J. K. Sailer, S. M. Patberg, K. Sandor, Y. Krishnan and M. G. Walter, *J. Am. Chem. Soc.*, 2019, **141**, 18780–18790.
70 A. Thorat, S. Behera, A. A. Boopathi and C. Kulkarni, *Angew. Chem., Int. Ed.*, 2024, **63**, e202409725.
71 B. Van Genabeek, B. F. M. De Waal, M. M. J. Gosens, L. M. Pitet, A. R. A. Palmans and E. W. Meijer, *J. Am. Chem. Soc.*, 2016, **138**, 4210–4218.
72 R. J. Kline, M. D. McGehee, E. N. Kadnikova, J. Liu, J. M. J. Fréchet and M. F. Toney, *Macromolecules*, 2005, **38**, 3312–3319.
73 T. Yamamoto, D. Komarudin, M. Arai, B.-L. Lee, H. Suganuma, N. Asakawa, Y. Inoue, K. Kubota, S. Sasaki, T. Fukuda and H. Matsuda, *J. Am. Chem. Soc.*, 1998, **120**, 2047–2058.